Relaxation dynamics and magnetic anisotropy in a low symmetry Dy(III) complex.

Eva Lucaccini,[a] Matteo Briganti,[a] Mauro Perfetti,[a,b] Laure Vendier,[c,d] Jean-Pierre Costes,[c,d] Federico Totti,*[a] Roberta Sessoli[a] and Lorenzo Sorace*[a]

Abstract: The magnetic behaviour of Dy(LH)$_3$ complex (where LH is the anion of 2-Hydroxy-N'-[(E)-(2-hydroxy-3-methoxyphenyl) methylidene] benzhydrazide) was analysed in depth both from the theoretical and experimental point of view. Cantilever Torque Magnetometry indicated that the complex has a Ising-type anisotropy, and provided two possible directions for the easy-axis of anisotropy due to the presence of two magnetically non equivalent molecules in the crystal. *Ab initio* calculations confirmed the strong Ising-type anisotropy and disentangled the two possible orientations. The results obtained by *ab initio* calculations were then used to rationalize the composite dynamic behaviour observed for both pure Dy(III) phase and the Y(III) diluted one, which showed two different relaxation channels in zero and non-zero static magnetic field. In particular, we showed that the relaxation behaviour in the higher temperature range can be correctly reproduced using a master matrix approach, which suggests that Orbach relaxation is going on through second excited doublet.

Introduction

The discovery of Ishikawa and co-workers [1] that a lanthanide bisphtalocyaninato molecule showed slow relaxation of the magnetization at low temperature, ignited large interest toward the dynamic of the magnetization of lanthanide-based complexes [2,3]. Following that seminal report, these systems (referred to as Single Ion Magnets) have indeed been proposed as candidates for application in high density data storage, molecular spintronics, and quantum information processing [4–7]. The origin of the peculiar magnetic behaviour of lanthanide ions lies in their strong magnetic anisotropy, stemming from the combined action of the spin-orbit coupling and the crystal field (CF) induced by the ligand(s) donor atoms, and by the large total angular momentum J (for the second half of the 4f series) [8]. These two features originate – when the two states with the largest projection of J are the ground ones – an anisotropy energy barrier for the reversal of the magnetization. In the absence of other efficient relaxation paths it is then possible to observe slow relaxation of the magnetization through an Orbach process, with the thermal dependence of the relaxation rate following an Arrhenius-like behaviour. This result requires both a highly symmetric axial disposition of the ligands around the lanthanide centre -

reducing the mixing between states with different M_J values - and a resulting ground state characterized by an M_J value as large as possible [9]. While it has been shown that complexes with lower symmetries can also possess axial eigenstates [10–12], in these situations it is not possible to predict *a priori* the composition of the ground state, since several different $|M_J\rangle$ can in principle contribute to it.

It has further been pointed out that the relaxation of the magnetization can be due to different mechanisms [13–15]. For example, at low temperature and for small values of applied magnetic field, quantum tunneling of magnetization (QT) can be strongly effective in accelerating the relaxation. In this sense, molecules containing Kramers' ions are clearly to be preferred, since in semi-classical approach QT is forbidden for semi-integer spins. However, this process can be mediated by dipolar and hyperfine interactions, so that in zero field fast relaxation of the magnetization is often observed. Suppression of the QT relaxation processes is then achieved by diluting paramagnetic complexes within an isostructural diamagnetic matrix, which reduces dipolar interactions, and/or by applying a static magnetic field. On increasing magnetic field the direct process gains importance due to the larger number of available phonons of correct energy and can become the dominant contribution [16]. Finally, relaxation may occur through a Raman process that gives a more marked temperature dependence of the magnetic relaxation time τ, since an interaction with phonons from the thermal bath and virtual energy states is involved [17]. It is quite clear that to correctly describe the relaxation processes in these systems a detailed picture of the electronic structure of the lanthanide ion and

[a] Dipartimento di Chimica "U. Schiff", Università di Firenze and INSTM RU, Via della Lastruccia 3-13, Sesto Fiorentino(FI), Italy. Tel: +39 0554573336; e-mail: federico.totti@unifi.it, lorenzo.sorace@unifi.it,

[b] Institut für Physikalische Chemie,Universität Stuttgart, Pfaffenwaldring 55, 70569 Stuttgart, Germany .

[c] Laboratoire de Chimie de Coordination 205, route de Narbonne 31077 Toulouse, Cedex 4, France.

[d] Université de Toulouse, UPS, INPT, F-31077, route de Narbonne 31077 Toulouse, Cedex 4, France.

its relation to the molecular structure is needed. An approach combining spectroscopic characterization (EPR, luminescence, Inelastic Neutron Scattering) and *ab initio* theoretical studies is now becoming the standard procedure for this scope [10, 18–22]. On the other hand single crystal magnetic measurements are still not much widespread [23, 24], despite they can cast light on the magnetic anisotropy by providing access to the preferred orientations of magnetization and on the degree of axiality of the low lying levels of the J-multiplet [25–27]. However, most crystal structures comprise symmetry related but magnetically non equivalent sites. In these cases single crystal magnetometry provides an averaged response and deconvolution of the different contributions to anisotropy is often impossible [28, 29]. On the other hand cantilever torque magnetometry (CTM), which only probes the anisotropic part of the magnetization, is less affected by this problem [29]. Further, its high sensitivity and the possibility to measure the magnetic anisotropy up to relatively high temperatures allows one to get an independent estimate of the gap between the ground and first excited doublet in lanthanide complexes [29, 30]. The outcome of this experimental characterization can then be used to validate the results of *ab initio* calculations that, on their turn, help to unravel the knot and to avoid misinterpretation of the observed dynamic behaviour by providing information on the eigenstate composition and the corresponding energy gaps. Following this strategy we present here a complete experimental characterization, obtained by X-ray diffractometry, Electron Paramagnetic Resonance (EPR) spectroscopy, single crystal CTM, *AC* and *DC* susceptibility flanked by theoretical analysis based on *ab initio* methods of a new mononuclear Dy complex behaving as Single Ion Magnet in zero field. The complex has been synthesized using a potentially pentadentate ligand: however, only three of its binding sites are used to bind to the Dy ion, thus resulting in a neutral molecule which is in principle sublimable [31].

Results and discussion

Synthesis and structure determination.   The 2-Hydroxy-N'-[(E)-(2-hydroxy-3-methoxyphenyl) methylidene] benzhydrazide ligand, LH_2 (Scheme 1), was obtained by reaction of 2-hydroxybenzohydrazide with pyridine carboxaldehyde, following the procedure reported in the Experimental Section. This is a potentially pentadentate ligand, which possesses two functional groups that can be deprotonated: its coordination chemistry has, up to now, only been investigated with regard to nickel or cobalt complexes [32]. Its complete characterization, including assignment
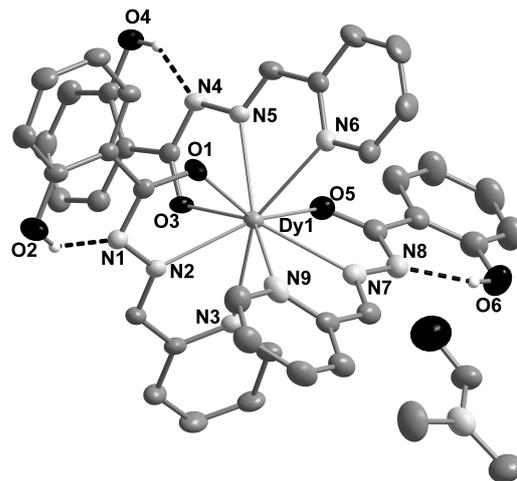

Figure 1: View of the asymmetric unit of **Dy**, including one molecule of the complex and one dmf molecule. The dashed lines evidence the three intramolecular hydrogen bonds stabilizing the structure. Remaining hydrogen atoms are not shown for clarity sake. Ellipsoids are drawn at 40% probability, with the exception of hydrogen atoms, for which ball and stick representation is used.

of 1D and 2D ^1H and ^{13}C NMR spectra and chemical analysis are also reported in Experimental Section, and are partially differing from those previously reported [32]. This LH_2 ligand reacts with $Dy(NO_3)_3$ in presence of piperidine to provide a yellow complex, which from analytical data and X-ray analysis (see below) is found to be neutral, the Dy(III) ion being coordinated to three monodeprotonated ligands. Molecular structure obtained by single crystal X-ray diffractometry indicates that $Dy(LH)_3$dmf (**Dy**) crystallizes in the monoclinic $P2_1/n$ space group. Its asymmetric unit (fig. 1) is made up of one mononuclear $[Dy(LH)_3]$ neutral molecule and one dimethylformamide (dmf) molecule. The Dy ion experiences a N_6O_3 coordination environment provided by the three tris-chelating LH ligands. The hydrazide function is deprotonated while the phenol function remains protonated and not involved in coordination with the Dy ion. Each ligand remains essentially planar, with the exception of the phenolic residues, due to the presence of an intramolecular hydrogen bond involving the non-deprotonated phenol function and the hydrazide nitrogen atom of each ligand. The Dy−N(pyridine) bond lengths, 2.574(3) Å to 2.696(4) Å, are slightly larger than the Dy−N(hydrazide) bond lengths, 2.496(3) Å to 2.538(4) Å, the shorter bonds involving the Dy−O of the hydrazone part of the ligand, 2.322(3) Å to 2.368(3) Å (selected bonds and angles are reported in Supplementary table S1). Analysis of the nine-coordinate DyN_6O_3 polyhedron with the SHAPE program [33] (see table S2) suggests that the coordination polyhedron is intermediate between the different pos-

sible choices for a nine coordination, with a slight preference for a spherical capped square antiprism. For this choice the capping atom is the N8 hydrazide nitrogen one, and the two squares of the antiprism are made up by the N9 N3 O5 N6 and O1 N2 O3 N5 atoms (fig. S1). The packing of the molecules in the lattice is such that the closest Dy-Dy intermolecular distance is 10.73 Å. Phenoxo- rings on molecules related by the inversion center are parallel: however the corresponding centroids are separated by 6.75 Å so that the corresponding $\pi - \pi$ stacking interactions are expected to be very weak [34].

Static magnetic properties. The static magnetic properties of a microcrystalline powder sample of **Dy** were investigated by means of DC measurements and the behaviour of the magnetization was studied both as a function of field H and temperature T. The χT vs T curve is reported in fig. S2: the room temperature experimental value ($\chi T = 13.97\,\text{emu}\,\text{K}\,\text{mol}^{-1}$) is consistent with the free ion expectation one for Dy(III) ($^6H_{15/2}$, $g_J = 4/3$, $\chi T = 14.17\,\text{emu}\,\text{K}\,\text{mol}^{-1}$). A smooth decrease is observed on lowering temperature, which is attributed to the depopulation of excited levels of the $^6H_{15/2}$ multiplet, split by the CF. The magnetization versus field was measured at 2 K and 4 K and it is reported in fig. S3. The saturation value is $5\mu_\text{B}$, as already observed for other molecular complexes containing Dy(III) [35, 36].

Study of the magnetic anisotropy. EPR spectroscopy is widely used to investigate magnetic anisotropy of Kramers' system, however in our case the complex revealed to be silent. This can be in principle attributed either to fast relaxation or to a low intradoublet transition probability due to the ground state composition, with the excited doublets being too high in energy to observe interdoublet transitions. The latter explanation points to a large axiality of the ground state which was then investigated by using CTM. This technique exploits the magnetic torque of a molecule immersed in a homogenous magnetic field and has already proven to be extremely useful to determine the anisotropic features of lanthanide-based Single Molecule Magnets [29, 30, 37]. In this experimental setup the variation of the capacitance of the capacitor, due to the deflection of the cantilever, is proportional to the magnetic torque experienced by the sample. This torque $\mathcal{T}$ is defined as the vector product between magnetization (M) and magnetic field (B). Experimentally, only the $\mathcal{T}_\text{Y}$ component of the torque that lies on the rotation axis (chosen as the Y axis of the XYZ laboratory reference frame) is detectable, thus we can write:

$$\begin{aligned}\mathcal{T}_\text{Y} &= M_\text{z}B_\text{x} - M_\text{x}B_\text{z} \\ &= B^2 \sin\varphi \cos\varphi (\chi_\text{zz} - \chi_\text{xx})\end{aligned} \quad (1)$$

where an additional $B^2(2\sin^2\varphi - 1)\chi_\text{xz}$ term was omitted because it is always possible to set it to zero by a proper shift of the rotation. In eq. 1, that is only valid for $g\mu_\text{B}S_\text{eff}B \ll k_\text{B}T$, χ_IJ are the components of the magnetic susceptibility tensor, while φ is the angle between the magnetic field B and the projection of the easy axis (z axis in the xyz molecular reference frame) on the rotation plane. This should not be confused with the rotation angle (the angle between the cantilever plane and the magnetic field direction), hereafter called θ. If B is increased enough eq. 1 breaks down and the torque curves assume a different shape if B is parallel or perpendicular to the easy direction of anisotropy, making possible the disentanglement of non collinear contributions. To reduce the effect of intermolecular interactions
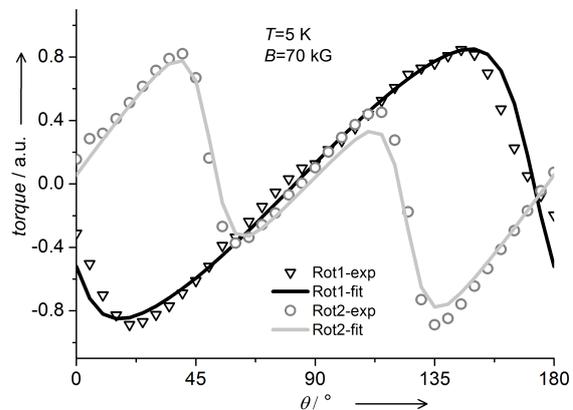

Figure 2: Torque curves for the two rotations in a magnetic field of 70 kG and at 5 K. The solid lines represent the best fit of the magnetic torque using parameters reported in the text; the symbols are the experimental data for Rot1 (empty squares) and Rot2 (empty circles).

and of demagnetizing fields due to shape anisotropy, we chose to use a sample of the isostructural Y(III) derivative doped with ca. 10 % Dy(III), hereafter **YDy**. Since this compound crystallizes in a monoclinic space group, $P2_1/n$, and the molecules do not sit on any symmetry element, the crystal anisotropy will be in general different from the molecular one. The orthogonal crystallographic reference frame in a monoclinic space group is abc^* and rotations in two orthogonal planes have been performed: in the first one (Rot1) the rotation is performed around b, while in the second one (Rot2) the rotation axis lies in the ac^* plane (see fig. S4 for detailed information on the reference frames and rotation geometries). Interestingly, in the first rotation all molecules in the unit cell provide the same contribution, being related by the two fold axis lying along b, while two families of differently oriented molecules are detected in the second rotation. We measured the torque signal at $T = 5\,\text{K}$ and $T = 10\,\text{K}$ with B ranging from 30 up to 70 kG.
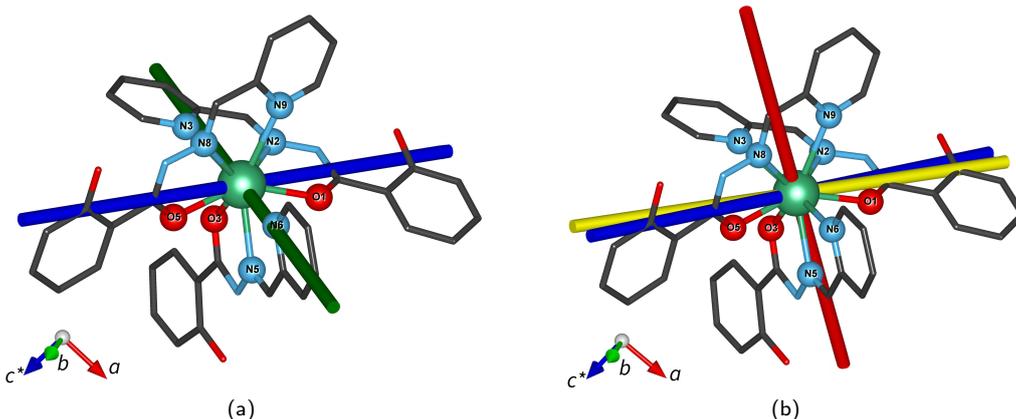
Figure 3: (a) two possible directions of the easy axis of magnetic anisotropy as determined by CTM: the blue one is substantially coincident with the calculated one (compare with fig. 3b). (b) direction of the easy axis anisotropy for the first three energy doublets: ground (blue), first excited (yellow), second excited (red) computed direction.

The resulting torque data were fitted by modelling the electronic structure of the **Dy** complex using an effective Spin-Hamiltonian:

$$\mathcal{H}_s = \mu_B \mathbf{S}_{\text{eff}} \cdot \boldsymbol{g} \cdot \mathbf{B} \qquad (2)$$

where $\boldsymbol{g}$ is the g-tensor, diagonal in the molecular reference frame, μ_B is the Bohr magneton and $\mathbf{S}_{\text{eff}}$ is an effective $S = 1/2$ spin operator.

To correctly reproduce the torque shape, three further parameters have to be taken into account: a scale factor (F_{sc}, that must be the same for all rotations) and two Euler angles, namely ρ and ξ (using the extrinsic $x-$convention), which describe the orientation of the molecular reference frame with respect to the crystallographic one. Indeed in the case of uniaxial anisotropy the third Euler angle is irrelevant. In fig. 2 we report an example of two torque curves measured at the same applied magnetic field and temperature for the two rotations (the complete set of experimental data and the corresponding fits are reported in SI, fig. S5). The fitting procedure gave the following best fit parameters: $g_x = g_y = 0.010(5)$, $g_z = 16(1)$, $\rho = 212(1)°$, $\xi = 71(1)°$ and $F_{\text{sc}} = 2.6(3) \times 10^{-2}$, thus indicating strong Ising character of the ground doublet. The resulting director cosines of the easy axis (z in molecular reference frame), with respect to abc^* are: $\cos \alpha_1 = -0.501$, $\cos \alpha_2 = 0.801$, $\cos \alpha_3 = 0.326$ ($\alpha_1 = 120°$, $\alpha_2 = 37°$ and $\alpha_3 = 71°$). Due to the presence of two magnetically non equivalent molecules in the unit cell these direction cosines can identify two possible orientations for the magnetic anisotropy axis with respect to the molecular structure, see fig. 3a. It is interesting to note that none of the two possibilities correlate with the highest symmetry axis (C_4 or C_3) of the best fit coordination polyhedra, capped square antiprism or tricapped trigonal prism (see fig. S1). This is in agreement with the fact that the idealized structural geometry does not take into account the heterolepticity of the complex, which results in a CF symmetry completely different from the structural one. A simple electrostatic model [38] has been used to calculate the orientation of the easy axis of magnetization: the angle between experimental (drawn as blue axis in in fig. 3a) and calculated direction resulted to be about 13° (see table S3-S4 and fig. S7). Since the error of a visual crystal alignment can be estimated to be about 5° (see Experimental Section) we can consider the calculated orientation to be in fair agreement with the experimental one. This confirms that the coordination environment of Dy(III) in the complex can provide a strong Ising character, but an accurate prediction of the orientation of the anisotropy axis, as well as an estimation of the low symmetry components of the CF, requires a more detailed approach.

Ab initio calculations. Since we had indications of the strong Ising character of the complex, we chose to perform an accurate *ab initio* characterization to get more detailed insights of the Dy(III) electronic structure. A first relevant test about the correct reproduction of experimental properties concerns the calculation of the orientation and magnitude of the magnetic anisotropy compared to the results of CTM. In agreement with the experimental CTM results the calculated ground Kramers' doublet shows an almost pure Ising character with a principal value of $g_z = 19.8$ (see table 1) and contribution from $M_J = \pm 15/2$ only. The computed easy axis orientation for the ground doublet (fig. 3b) approximately lies on the line connecting two carbonyl oxygens of two LH ligands ($\cos \alpha_1 = -0.531454$, $\cos \alpha_2 = 0.788731$, $\cos \alpha_3 = 0.308967$). It is evident that the calculated direction is almost coincident with one of the two possible choices provided by the CTM analysis (see

above and fig. 3a), the angle formed by calculated and experimental orientation being 2.9°, which is below the estimated experimental uncertainty (5°). Interestingly, the quality of the fit is not very sensitive to the actual magnitude of the g_z value, as long as the system has strong Ising character (i.e. $g_z > 15$, $g_x, g_y < 1$), while it depends strongly on the Euler angles values. As a consequence, if the torque fit is performed keeping the g−values fixed to the computed ones ($g_z \sim 20$) the Euler angles are not affected (see fig. S6). The calculated *ab initio* anisotropic properties are then perfectly consistent with the results of the CTM investigation. With this proof of the reliability of *ab initio* calculations we used the set of calculated Stevens' Spin Hamiltonian parameters [39] (see table S5) pertaining to the ground $J = 15/2$ state to simulate the static magnetic properties of the complex using the home-developed software EVALUCF [13]. In particular, while the correct simulation of the M *vs* H curves at low temperature confirms that the ground doublet properties are well reproduced by *ab initio* calculations, an indication about the correct evaluation of energy splitting and eigenstates of the ground $J = 15/2$ state can be provided by the simulation of the χT *vs* T curve. For this quantity, the agreement between experimental and calculated curve (see fig. S2), apart for a small scaling factor within experimental error ($< 5\,\%$), lends further support to the electronic structure obtained by *ab initio* calculations. This is reported in term of computed energy splitting [39] between the Kramers' doublets and of their composition (M_J contributions larger that 0.1) in fig. S8. The calculated energy separation between ground state with the first and the second excited state is 195 and 237 cm^{-1}, respectively. The first ex-

Table 1: Results of the calculations with RCC basis sets for **Dy**: energy splitting of the ground $^6H_{\frac{15}{2}}$ multiplet and principal values of the corresponding g tensor for each Kramers' doublet. See table S6 for the calculated splitting of the first excited multiplet $^6H_{\frac{13}{2}}$.

	Energy Levels	(cm^{-1})	g_x	g_y	g_z
	E_0	0	0.0	0.0	19.8
	E_1	195	0.5	1.8	14.9
	E_2	237	0.1	2.2	14.3
$^6H_{\frac{15}{2}}$	E_3	289	1.5	3.7	12.1
	E_4	324	0.6	2.8	13.8
	E_5	371	2.6	4.5	8.8
	E_6	430	3.4	4.1	7.4
	E_7	478	1.1	4.7	15.9

cited doublet shows a prominent contribution from the $\pm 13/2$ components with only the $\pm 11/2$ and $\pm 7/2$ ones as minor contributions, which are nevertheless enough to induce appreciable deviations from the ax-

iality of the **g** tensor. A much larger mixing among different M_J components is observed for the third excited doublet, while for the fifth excited doublet the axiality is completely lost. It is to be stressed that in addition to the increased rhombicity, the non-collinearity of the easy axis with respect to the one of the ground state is also increasing with the energy of the doublets (see table S7 and fig. 3b). Indeed the easy axis of the ground doublet forms an angle of 6° with the easy axis of the first excited doublet and of about 60° with the one of the second excited doublet. In this framework, the calculations suggest that if magnetic relaxation occurs only via an Orbach two-phonon mechanism, this should likely involve the second excited state. In such a case the energy barrier to be overcome would be of the order of 330 K, thus indicating the possible observation of an overall slow relaxation rate at relatively high temperatures.

Dynamic magnetic properties. To have more insights on this important point, the dynamic magnetic properties of **Dy** were investigated performing AC magnetic susceptibility experiments, as a function of frequency (0.02 Hz to 10 000 Hz), temperature, and of DC applied field (see fig. S9-S12). This investigation revealed a composite dynamic magnetic behaviour between 2 and 20 K. The pure complex showed two different relaxation channels in zero and non-zero magnetic static field: the application of an external field allows to suppress one channel and activate the other one (see fig. 4). Further, field dependent
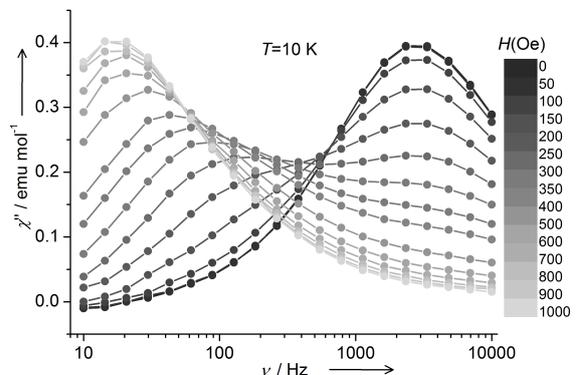

Figure 4: Imaginary susceptibility of **Dy** at 10 K as a function of the applied field.

measurements performed at 2 K pointed out that the slow relaxation process reaches a minimum rate for $H_{DC} = 1000\,\mathrm{Oe}$, whereas for higher field the rate starts to increase back. This led us to choose this field for the measurements under external field. This behaviour is reminiscent of what previously reported by some of us for Dy(DOTA) derivative as well as other SMMs [35, 40–43]. The imaginary susceptibility curves χ'' in zero and applied field were fitted according to a Debye model [44, 45] and the corre-
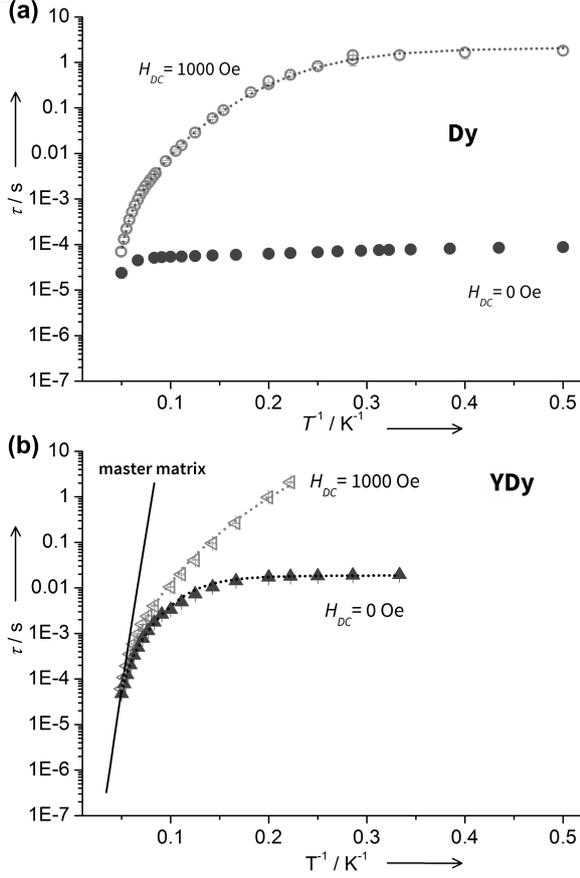
Figure 5: (a): relaxation times versus T^{-1} for compound **Dy**, in zero (full circles) and applied static field (empty ones). The relaxation in zero field is almost temperature independent up to 12 K. The grey dotted lines represents the best fit curve with $\Delta = 270$ K. (b): Relaxation times versus T^{-1} for compound **YDy**, in zero (full triangles) and applied static field (empty triangles). The dotted lines represent the fit of the relaxation time (see eq. 3) with $\Delta = 270$ K, the solid line is the relaxation time simulated using the master matrix equation.

sponding relaxation times versus T^{-1} is reported in fig. 5a. We notice that the relaxation rate of the channel dominating in zero field is almost temperature independent up to 12 K. Above this temperature it starts to increase with temperature like the one observed for the relaxation channel activated with an applied magnetic field. Such a trend is present up to 20 K where they become too fast to be measured. On the other hand, the rate observed for the relaxation channel activated by applying a magnetic field is clearly temperature dependent even at lower temperatures (see fig. 5a and fig. S11-S12). As a whole, this behavior suggests that the dominant process in zero field is directly related to QT of magnetization, whereas the slower one, occurring in applied field, is dominated by thermally activated relaxation. The curved nature of the Arrhenius plot for the relaxation

time in field, however, clearly points to a combination of processes contributing to the relaxation, including the persistence of a temperature independent process at the lowest temperatures [13].

In order to clarify if the intermolecular (dipolar) interactions between magnetic centres play any role in this behaviour, we have repeated the investigation of the dynamics on a magnetically diluted sample **YDy**. Its χT *vs* T curve is reported in fig. S2, evidencing the same temperature behaviour of the pure compound. The concentration of Dy(III) in the isomorphous Y(III) was estimated from the factor necessary to rescale the magnetization versus field curves at low temperature onto the magnetization curves of **YDy** (see fig. S3), providing a value of 10.5 %. Even in the diluted sample, two different relaxation channels were found to contribute to relaxation in zero and applied field (see fig. S13-S16). For **YDy** the relaxation of magnetization is however characterized by a much longer relaxation time τ, which reaches a few seconds at 4.5 K. Accordingly, at 2 K the diluted sample exhibited a butterfly shaped hysteresis (see fig. S17), that is no longer visible above 4 K. The observed temperature dependence of the relaxation rate of **YDy** for both relaxation channel was reproduced by including three contributions, a Raman and an Orbach process and a temperature independent process [19, 46–48]:

$$\tau^{-1} = CT^n + \tau_0^{-1}\exp(-\Delta/T) + B \qquad (3)$$

We performed a simultaneous fit of the relaxation time in field and in zero field (the corresponding parameters being indicated by *f* and *zf*, respectively, in the following), using the same set of parameters for Orbach process (τ_0 and Δ), while the Raman contribution was left free to vary for the two situations. This was intended to account for the possible contribution of direct process in the case of in-field measurements, which may affect the best fit value obtained for the Raman relaxation. A first attempt was made by fixing the value for the energy barrier Δ at 270 K $\sim$ 195 cm^{-1}, that is the energy of the first excited doublet computed by *ab initio* calculations. With this precondition we obtained the following values for the best-fit parameters: $\tau_0 = 1.3(2) \times 10^{-10}$ s, $n_f = 6.19(4)$, $C_f = 5.0(5) \times 10^{-5}$ s^{-1}K^{-n}, $B_f = 0$ (fixed), $n_{zf} = 5.5(2)$, $C_{zf} = 6(4) \times 10^{-4}$ s^{-1}K^{-n}, $B_{zf} = 53(2)$ s^{-1}. In a second step the Δ parameter was left free to vary, providing as best fit values $\tau_0 = 1(2) \times 10^{-11}$ s, $\Delta = 318(44)$ K (ca. 230 cm^{-1}), $n_f = 6.22(4)$, $C_f = 4.7(5) \times 10^{-5}$ s^{-1}K^{-n}, $B_f = 0$ (fixed), $n_{zf} = 5.6(2)$, $C_{zf} = 5(3) \times 10^{-4}$ s^{-1}K^{-n}, $B_{zf} = 53(2)$ s^{-1} (see also fig. S18). It is clear from these results that while at low temperature Raman and QT dominate the relaxation, the Orbach process is active in promoting the relaxation in the high temperature regime. It is however not completely clear

whether the latter process occurs via the first or the second excited doublet. As for the obtained τ_0 values, it is well known that for an Orbach process τ_0 should be $(10^{-3} \div 10^5)\Delta^{-3}$ (Δ expressed in K) [49]: substituting the two different values for Δ yields τ_0 in line with findings. Moreover, even if only qualitatively, the differences in τ_0 values are consistent with expectations, τ_0 being smaller in the case of larger Δ.

To obtain some more hints on the mechanism of the single-ion relaxation, transition moments between the states were computed [9, 50] (see fig. 6). On the basis of these transition moments no efficient QT relaxation is expected for the ground Kramers' doublet: the underestimation of the probability of QT relaxation by transition moments with respect to the experimental results is clearly due to the fact that this method takes into account only purely electronic, single molecular properties, whereas zero-field QT in Kramers' systems needs residual dipolar interactions and hyperfine coupling to occur (in the present case the magnetic nuclei are Dy(^{161}Dy, rel. ab.$= 18.9\,\%$ and ^{163}Dy, rel. ab.$= 24.9\,\%$, both with $I = 5/2$) [51]. On the basis of the *ab initio* results a thermally assisted QT is likely to occur already for the first excited state. However, the magnetic moment matrix element computed for a quantum tunneling mechanism between the two components of the first excited Kramers' doublet, $|1; \pm\rangle$, suggests that this is not the most likely process to occur. Indeed, from the first excited state both Orbach and thermally assisted QT processes are more probable: the former provides access to the second excited state while the latter would allow a reversal of the magnetization. On the basis of the above considerations a relaxation via the second excited state ($E_2 = 237\,\text{cm}^{-1}$) seems to be more likely, in fairly good agreement with the phenomenological value of the above reported value of the energy barrier of $230\,\text{cm}^{-1}$.

The use of transition moments to evaluate the potential relaxation paths is still providing only semi-quantitative indications [14, 52], despite being increasingly used in rationalizing the spin dynamics. A more directly quantitative reproduction of the observed dynamics, using the electronic structure derived by *ab initio* calculations, can be obtained by a master matrix based approach. [45].

This approach assumes a series of steps of the direct process type promoted by a suitable spin phonon coupling Hamiltonian, assumed here of the Villain type [45] for the sake of simplicity. Indeed in the low symmetry of our system the dynamic spin phonon coupling Hamiltonian proposed in Abragam and Bleaney textbook [49] would require the calculation of a huge number of CF Hamiltonians following different distortions [53] and is thus unfeasible. On the other hand,

notwithstanding its simplicity, our approach allows us to extract the relaxation time by calculating the relaxation rate γ_q^p from a state $|q\rangle$ (eigenstate of the Hamiltonian that describes the system) to another state $|p\rangle$:

$$\gamma_q^p = \frac{3v}{\pi\hbar^4 mc_s^5}\frac{(E_p - E_q)^3}{\exp\left[\beta(E_p - E_q)\right] - 1}$$
$$\left\{|\tilde{D}_a|^2\left[|\langle p|\mathbf{J}_+^2|q\rangle|^2 + |\langle p|\mathbf{J}_-^2|q\rangle|^2\right] + \right.$$
$$\left.|\tilde{D}_b|^2\left[|\langle p|\{\mathbf{J}_+,\mathbf{J}_z\}|q\rangle|^2 + |\langle p|\{\mathbf{J}_-,\mathbf{J}_z\}|q\rangle|^2\right]\right\}$$
(4)

where β is $1/k_\text{B}T$, v and m are the volume and the mass of the unit cell, $\tilde{D}_a$ and $\tilde{D}_b$ are the spin-phonon coupling parameters. If the energy levels and the eigenstates are known, the only parameters that need to be adjusted are the spin-phonon coupling parameters and $v/(mc_s^5)$. In our case the CF eigenfunctions of the ground J multiplet and the corresponding eigenvalues in zero applied field obtained by the *ab initio* calculations were used to obtain the Crystal Field matrix as $\mathbf{R}^T\mathbf{VR}$ (where $\mathbf{R}$ is the eigenfunctions matrix and $\mathbf{V}$ the diagonal matrix of the corresponding eigenvalues). The complete Hamiltonian (Crystal field + Static magnetic field) was then obtained by adding the Zeeman interactions in the $|M_J\rangle$ basis. After diagonalization this provided new eigenvalues and eigenfunctions by which it was possible to calculate the master matrix $\mathbf{\Gamma}$ for all the investigated temperatures. Diagonalization of the master matrix allowed to extract the relaxation time as $\tau = -1/\lambda_1$, where λ_1 is the first non vanishing eigenvalue of the master matrix. The result, obtained by adjusting both the spin-phonon coupling parameter to 0.05 and the pre-factor $(3v/\pi\hbar^4 mc_s^5)$ to 3000, is shown in fig. 5b. It is evident that while this approach reproduces the linear high temperature region above $15\,\text{K}$, being consistent with an energy barrier of about $320\,\text{K}$, it overestimates the relaxation time at lower temperature. This is a common feature for many lanthanide based-molecular magnets and is usually attributed to the higher effectiveness of Raman process at lower temperatures. This process is however quite elusive since the corresponding parameters are usually considered as phenomenological [13, 19, 46, 47, 54–56]. Indeed, to the best of our knowledge, no reports are available relating the values of the Raman parameters (C and n) obtained by fit of dynamic data to the structure of the investigated molecule. This is a severe drawback in the search of increased relaxation times for potential applications, since this process, which provides a channel of relatively fast relaxation even at quite low temperature, is currently beyond our control. It is however to be stressed that, despite the phenomenological fit of the temperature dependence of the relaxation rate pointed to the existence of a
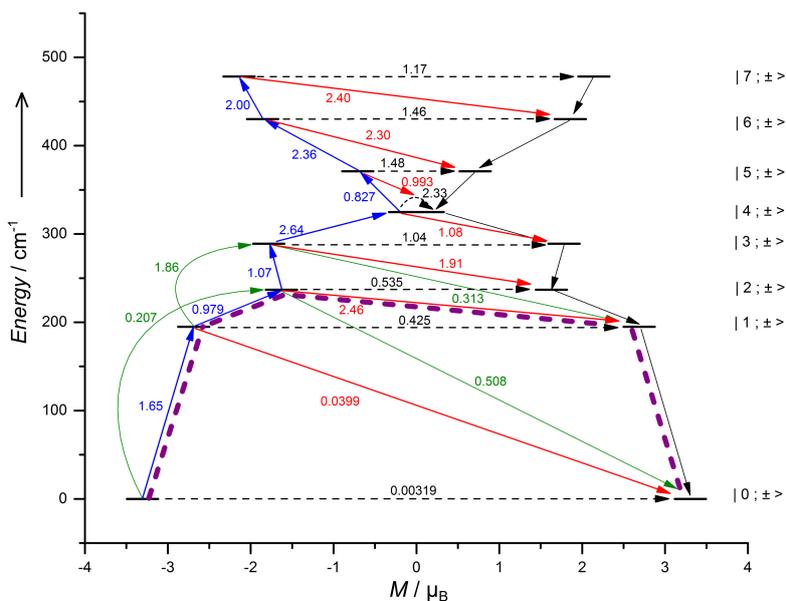
Figure 6: The *ab initio* computed magnetization blocking barrier for **Dy**. The thick black lines indicates the Kramers' doublets as a function of the projection of the magnetic moment on the chosen quantization axis (the one of ground multiplet). The red arrows show the possible pathways of the Orbach process. The dotted black arrows represent the presence of (thermal assisted) quantum tunneling between the connecting states. The numbers reported for each arrow are the mean absolute value for the corresponding matrix element of transition magnetic moment. The dotted purple lines show the most probable relaxation pathways for the reversal of magnetization.

T^n contribution, we cannot even be sure that this is associated to a real Raman process. Indeed, interactions which are not taken into account by the model, such as hyperfine and residual dipolar intermolecular interactions, may open the possibility of relaxation via quantum tunneling, and might also change the expected field and temperature dependence of direct processes [57].

Conclusions

In conclusion, we have presented a comprehensive experimental and theoretical investigation of the anisotropy and dynamic behaviour of a novel mononuclear lanthanide-based single molecule magnet. We evidenced that detailed cantilever torque magnetometry, which can be used more generally - in terms of crystal symmetry and size - than single crystal magnetometry, can provide independent confirmation of the results of *ab initio* calculations in the absence of further spectroscopic information. This is particularly relevant in case the system is EPR silent and no detailed luminescent data are available. In turn this allows to analyze the observed dynamics of the magnetization on the basis of the calculated electronic structure of the lanthanide center. For the studied complex the experimental and theoretical results indicate a strong axiality of both the ground doublet and the first excited state; the *ab initio* prediction of an

almost complete collinearity of the ground and first excited doublet is mirrored by the low temperature slow relaxation of the magnetization of the complex, which could be phenomenologically modelled by a combination of an Orbach and a Raman process. The observed behaviour could be qualitatively rationalized via the commonly used transition probabilities provided by the *ab initio* suite [9,50]. In addition to this we showed that the relaxation behaviour in the higher temperature range can be correctly reproduced assuming the *ab initio* computed electronic structure in a statistical analysis based on the master matrix approach. On the other hand, further processes are clearly contributing at low temperature, resulting in an experimental relaxation rate which is much faster than predicted by this approach. This might be due either to a true Raman process or to the unaccounted hyperfine and dipolar intermolecular interactions,the latter reduced but not completely quenched by the doping level used here. As a whole these results outline the necessity of a virtuous interplay between detailed single crystal studies and *ab initio* calculations. This process allowed us to obtain a detailed understanding of the relation between the electronic structure and the rich low temperature magnetization dynamics in this system, a point of crucial importance for rationally improving the properties of lanthanide-based single molecule magnets.

Experimental setup

Synthesis. $Dy(NO_3)_3 \cdot 5\,H_2O$, $Y(NO_3)_3 \cdot 5\,H_2O$, pyridine carboxaldehyde, piperidine (Aldrich) were used as purchased. 2-hydroxybenzohydrazide was prepared as previously described [58]. High-grade solvents (diethyl ether, dimethylformamide (dmf), methanol) were used for the syntheses of ligands and complexes.

2-Hydroxy-N'-[(E)-(2-hydroxy-3-methoxyphenyl) methylidene]benzhydrazide. Addition of pyridine carboxaldehyde ($1.07\,g$, $1.0 \times 10^{-3}\,mol$) to a stirred MeOH solution ($30\,mL$) of 2-hydroxybenzhydrazide ($1.52\,g$, $1.0 \times 10^{-3}\,mol$) followed by a thirty minutes heating induced formation of a bulky white precipitate that was filtered off after cooling, washed with MeOH, diethyl ether and dried. Yield: $2.7\,g$ ($95\,\%$). Anal. Calc. for $C_{13}H_{11}N_3O_2$ ($241.2\,g\,mol^{-1}$): C, 64.7; H, 4.6; N, 17.4. Found: C, 64.4; H, 4.5; N, 17.2 %. ^{1}H NMR (400 MHz, dmso-d_6): δ(ppm) 6.99 (t+d, J=7 Hz, 2 H, CH−3 + CH−5), 7.45 (t+d, J=7.5 Hz, 5 H, CH−4 + CH−4'), 7.89 (t+d, J= 7.5 Hz, 2 H, CH−5' + CH−6'), 8.00 (d, J=7 Hz, 1 H, CH−6), 8.49 (s, 1 H, HC=N), 8.64 (d, J=7 Hz, 1 H, CH−3'), 11.71 (s, 1 H, NH), 12.1 (s, 1 H, OH). ^{13}C NMR (100.63 MHz, dmso-d_6): 116.65 (s, ArC−1), 117.71 (s, ArC−3), 119.44 (s, ArC−5), 120.53 (s, ArC−6'), 125.01 (s, ArC−4'), 129.14 (s, ArC−6), 134.36 (s, ArC−4), 137.37 (s, ArC−5'), 120.53 (s, ArC−6'), 149.16 (s, ArC−3'), 150.02 (s, NC=N), 153.54 (s, ArC−6'), 165.44 (s, OCNH).
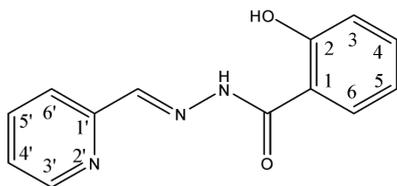
Scheme 1: LH$_2$ ligand with numbering scheme retained for NMR data (^{1}H and ^{13}C).

Dy(LH)$_3$ (Dy). Addition of piperidine ($0.17\,g$, $2.0 \times 10^{-3}\,mol$) to a stirred dmf solution ($10\,mL$) of the above ligand ($0.27\,g$, $1.0 \times 10^{-3}\,mol$) and $Dy(NO_3)_3 \cdot 5\,H_2O$ ($0.43\,g$, $1.0 \times 10^{-3}\,mol$) induced appearance of a more intense yellow solution. The solution was filtered off and set aside. The crystals that appeared twelve days later were isolated by filtration and dried. Yield: $0.16\,g$ ($50.5\,\%$). Anal. Calc. for $C_{42}H_{37}DyN_{10}O_7$ ($956.32\,g\,mol^{-1}$): C, 52.75; H, 3.90; N, 14.65 %. Found: C, 52.45; H, 3.78; N, 14.43 %. IR (ATR): 3448l, 3065w,2991w, 2925w, 2875w, 2792w, 2705w, 2610w,1681w, 1667m, 1599m, 1586m, 1561m, 1520m, 1488m, 1474m, 1452m, 1417w, 1357s, 1346s, 1302m, 1252m, 1230w, 1147m, 1090w, 1065m, 1008w, 926w, 866w, 830w, 760m, 740w, 702w, 689w, 658w, 632w cm^{-1}.

YDy(LH)$_3$. Use of the same experimental process with $Y(NO_3)_3 \cdot 5\,H_2O$ ($0.36\,g$, $2.0 \times 10^{-3}\,mol$) along with 30 mg of $Dy(NO_3)_3 \cdot 5\,H_2O$ yielded crystals that were isolated by filtration and dried. Yield: $0.19\,g$ ($64.7\,\%$).

IR (ATR): 3440l, 3068w, 2929w, 2775w, 2718w, 2612w, 1663w, 1598m, 1584m, 1562m, 1519m, 1484m, 1472m, 1454m, 1426w, 1362s, 1349s, 1297m, 1246m, 1227w, 1156m, 1146m, 1100w, 1066m, 1042w, 1028w, 1008w, 921w, 866w, 830w, 757m, 741w, 703w, 689w, 680w, 633w cm^{-1}.

Elemental analyses were carried out at the Laboratoire de Chimie de Coordination Microanalytical Laboratory in Toulouse, France, for C, H, and N. IR spectra were recorded on a Spectrum 100 FT-IR Perkin-Elmer spectrophotometer using the ATR mode.

Crystallographic Data Collection and Structure Determinations. Crystals of **Dy** were kept in the mother liquor until they were dipped into oil. The chosen crystals were mounted on a Mitegen micromount and quickly cooled down to 180 K. The selected crystals of **Dy** (yellow, $0.18 \times 0.10 \times 0.04$ mm^3) were mounted on a Oxford Diffraction Xcalibur diffractometer using a graphite-monochromated Mo K$_\alpha$ radiation ($\lambda = 0.710\,73$ Å) and equipped with an Oxford Instrument Cooler Device. Data were collected at low temperature (180 K). The final unit cell parameters have been obtained by means of least-squares refinements. The structures have been solved by Direct Methods using SIR92 [59], and refined by means of least-squares procedures on a F^2 with the program SHELXL97 [60], included in the software package WinGX version 1.63 [61]. The Atomic Scattering Factors were taken from International tables for X-Ray Crystallography [62]. All non-hydrogen atoms were anisotropically refined, and in the last cycles of refinement a weighting scheme was used, where weights are calculated from the following formula: $w = 1/[\sigma^2(Fo^2) + (aP)^2 + bP]$ where $P = (Fo^2 + 2Fc^2)/3$. CCDC-1433866 contains the crystallographic data for **Dy**. These data can be obtained free of charge from The Cambridge Crystallographic Data Centre via www.ccdc.cam.ac.uk/data_request/cif.

Crystal data for Dy. $C_{42}H_{37}DyN_{10}O_7$, M = $956.32\,g\,mol^{-1}$, monoclinic $P2_1/n$, Z = 4, $a = 9.8585(3)$ Å, $b = 22.1870(6)$ Å, $c = 19.1215(5)$ Å, $\alpha = \gamma = 90°$, $\beta = 94.160(3)°$, $V = 4171.3(2)$ Å^3, 35 087 collected reflections, 8511 unique reflections ($R_{int} = 0.0416$), R-factor = 0.0368, weighted R-factor = 0.0921 for 6996 contributing reflections [I > 2σ(I)].

Magnetic characterization. The purity of the polycrystalline powders of (**Dy**) used for magnetic characterization was checked with a Bruker D8 Advance powder diffractometer equipped with a Cu source (K$_\alpha$, $\lambda = 1.54$ Å) (see fig. S19). The isomorphicity of the diluted compound **YDy** with the pure one was checked with a Single Crystal diffractometer Xcalibur3 equipped with a Mo source (K$_\alpha$, $\lambda = 0.71$ Å). Xcalibur3 is a 4 cycles kappa geometry diffractometer equipped with a Sapphire 3 CCD detector.

DC magnetic measurements were performed by using a Quantum Design MPMS SQUID magnetometer on powders pressed in a pellet to avoid field induced orientation of the crystallites. The concentration of Dy in Y diluted sample was estimated by superimposing the magnetization curve versus field of pure and diluted compound at low temperature. *AC* susceptibility was measured using Quantum Design PPMS in *AC* mode for the frequency range

10 to 10^4 Hz. The Quantum Design MPMS SQUID magnetometer was used for low frequencies (0.02 to 10^3 Hz).

EPR spectra were recorded at 3 K and 5 K with a E500 Bruker spectrometer for the X band ($\nu \sim 9.4$ GHz).

The CTM measurements were performed using a home made two legs CuBe cantilever separated by 0.1 mm from a gold plate. The cantilever was inserted in an Oxford Instruments MAGLAB2000 platform with automated rotation of the cantilever chip in a vertical magnet. The capacitance of the cantilever was detected with a Andeen-Hegerling2500 A Ultra Precision Capacitance Bridge. Faces of the measured crystal were indexed by X-ray diffraction using the above described setup and then fixed on the cantilever with glue. This procedure results in an estimated uncertainty on the actual orientation of the crystal of about $5°$.

***Ab initio* calculations**. The quantum chemistry package MOLCAS 8.0 [63] was employed in all the calculations. X-ray structure resolved from the diffraction pattern recorded at 180 K was used throughout the study. All atoms were described with standard all electrons ANO-RCC basis set. TZP basis set was employed for dysprosium, nitrogen and oxygen atoms (see table S8). DZP and DZ for Carbon and Hydrogen atoms. respectively. The default contraction scheme was not altered. The Douglass-Kroll-Hess hamiltonian was employed in order to take into account scalar relativistic effects. The spin-free wave functions were obtained with the Complete Active Space Self Consistent Field (CASSCF) method for a state-average calculation of all roots arising from the considered active space. The active space consisted of nine electrons in the seven f orbitals of the lanthanide atom [CASSCF(9,7)]. The Spin-Orbit interaction was considered in the following Restricted Active Space State Interaction (RASSI) calculation by mixing all the state-averaged obtained 21 sextuplets. The g-tensor for every Kramers doublet and his orientation in the molecular frame, the crystal-field parameters and their decomposition in wavefunctions with definite projection of the total moment $|J, M_J\rangle$ were computed with the SINGLE_ANISO package. The quantization axis was chosen to be the main magnetic axis of the ground doublet.

Acknowledgements

References

[1] N. Ishikawa, M. Sugita, T. Ishikawa, S.-y. Koshihara, Y. Kaizu, *J. Am. Chem. Soc.* **2003**, *125*, 8694–8695.

[2] R. Layfield, M. Murugesu (Eds.), *Lanthanides and Actinides in Molecular Magnetism*, John Wiley & Sons, **2015**.

[3] C. Benelli, D. Gatteschi, *Introduction to Molecular Magnetism: From Transition Metals to Lanthanides*, John Wiley & Sons, **2015**.

[4] R. Vincent, S. Klyatskaya, M. Ruben, W. Wernsdorfer, F. Balestro, *Nature* **2012**, *488*, 357–360.

[5] F. Habib, M. Murugesu, *Chem. Soc. Rev.* **2013**, *42*, 3278–3288.

[6] G. Aromí, D. Aguila, P. Gamez, F. Luis, O. Roubeau, *Chem. Soc. Rev.* **2012**, *41*, 537–546.

[7] J. D. Rinehart, J. R. Long, *Chem. Sci.* **2011**, *2*, 2078–2085.

[8] L. Sorace, D. Gatteschi in *Lanthanides and Actinides in Molecular Magnetism*, R. Layfield, M. Murugesu (Eds.), John Wiley & Sons, **2015**, chapter 1.

[9] L. Ungur, L. F. Chibotaru, *Phys. Chem. Chem. Phys.* **2011**, *13*, 20086–20090.

[10] G. Cucinotta, M. Perfetti, J. Luzon, M. Etienne, P.-E. Car, A. Caneschi, G. Calvez, K. Bernot, R. Sessoli, *Angew. Chem. Int. Ed.* **2012**, *51*, 1606–1610.

[11] N. F. Chilton, S. K. Langley, B. Moubaraki, A. Soncini, S. R. Batten, K. S. Murray, *Chem. Sci.* **2013**, *4*, 1719–1730.

[12] D. Aravena, E. Ruiz, *Inorg. Chem.* **2013**, *52*, 13770–13778.

[13] E. Lucaccini, L. Sorace, M. Perfetti, J.-P. Costes, R. Sessoli, *Chem. Commun.* **2014**, *50*, 1648–1651.

[14] R. J. Blagg, L. Ungur, F. Tuna, J. Speak, P. Comar, D. Collison, W. Wernsdorfer, E. J. McInnes, L. F. Chibotaru, R. E. Winpenny, *Nature Chem.* **2013**, *5*, 673–678.

[15] J.-L. Liu, K. Yuan, J.-D. Leng, L. Ungur, W. Wernsdorfer, F.-S. Guo, L. F. Chibotaru, M.-L. Tong, *Inorg. Chem.* **2012**, *51*, 8538–8544.

[16] L. Tesi, E. Lucaccini, I. Cimatti, M. Perfetti, M. Mannini, A. Matteo, E. Morra, M. Chiesa, A. Caneschi, L. Sorace, R. Sessoli, *Chem. Sci.* **2015**, 10.1039/C5SC04295J.

[17] T. Fukuda, N. Shigeyoshi, T. Yamamura, N. Ishikawa, *Inorg. Chem.* **2014**, *53*, 9080–9086.

[18] R. Marx, F. Moro, M. Dorfel, L. Ungur, M. Waters, S. D. Jiang, M. Orlita, J. Taylor, W. Frey, L. F. Chibotaru, J. van Slageren, *Chem. Sci.* **2014**, *5*, 3287–3293.

[19] Y. Rechkemmer, J. E. Fischer, R. Marx, M. Dörfel, P. Neugebauer, S. Horvath, M. Gysler, T. Brock-Nannestad, W. Frey, M. F. Reid, , J. van Slageren, *J. Am. Chem. Soc.* **2015**, *137*, 13114–13120.

[20] S. I. Klokishner, S. M. Ostrovsky, O. S. Reu, A. V. Palii, P. L. Tregenna-Piggott, T. Brock-Nannestad, J. Bendix, H. Mutka, *J. Phys. Chem. C* **2009**, *113*, 8573–8582.

[21] J. Long, J. Rouquette, J.-M. Thibaud, R. A. Ferreira, L. D. Carlos, B. Donnadieu, V. Vieru, L. F. Chibotaru, L. Konczewicz, J. Haines, Y. Guari, J. Larionova, *Angew. Chem. Int. Ed.* **2015**, *54*, 2236–2240.

[22] E. M. Pineda, N. F. Chilton, R. Marx, M. Dörfel, D. O. Sells, P. Neugebauer, S.-D. Jiang, D. Collison, J. van Slageren, E. J. McInnes, R. E. Winpenny, *Nature Commun.* **2014**, *5*.

[23] L. Sorace, C. Sangregorio, A. Figuerola, C. Benelli, D. Gatteschi, *Chem. Eur. J.* **2009**, *15*, 1377–1388.

[24] J. J. Baldoví, J. M. Clemente-Juan, E. Coronado, A. Gaita-Ariño, *Inorg. Chem.* **2014**, *53*, 11323–11327.

[25] J. Jung, F. Le Natur, O. Cador, F. Pointillart, G. Calvez, C. Daiguebonne, O. Guillou, T. Guizouarn, B. Le Guennic, K. Bernot, *Chem. Commun.* **2014**, *50*, 13346–13348.

[26] K. Bernot, J. Luzon, L. Bogani, M. Etienne, C. Sangregorio, M. Shanmugam, A. Caneschi, R. Sessoli, D. Gatteschi, *J. Am. Chem. Soc.* **2009**, *131*, 5573–5579.

[27] M.-E. Boulon, G. Cucinotta, J. Luzon, C. Degl'Innocenti, M. Perfetti, K. Bernot, G. Calvez, A. Caneschi, R. Sessoli, *Angew. Chem. Int. Ed.* **2013**, *52*, 350–354.

[28] A. Cornia, D. Gatteschi, R. Sessoli, *Coord. Chem. Rev.* **2001**, *219*, 573–604.

[29] M. Perfetti, G. Cucinotta, M.-E. Boulon, F. El Hallak, S. Gao, R. Sessoli, *Chem. Eur. J.* **2014**, *20*, 14051–14056.

[30] M. Perfetti, E. Lucaccini, L. Sorace, J.-P. Costes, R. Sessoli, *Inorg. Chem.* **2015**, *54*, 3090–3092.

[31] X. Yi, K. Bernot, F. Pointillart, G. Poneti, G. Calvez, C. Daiguebonne, O. Guillou, R. Sessoli, *Chem. Eur. J.* **2012**, *18*, 11379–11387.

[32] P. Zhou, Y.-G. Zhao, Y. Bai, K.-L. Pang, C. He, *Inorg. Chim. Acta* **2007**, *360*, 3965–3970.

[33] M. Llunell, D. Casanova, J. Cirera, J. Bofill, P. Alemany, S. Alvarez, M. Pinsky, D. Avnir **2003**.

[34] C. Janiak, *J. Chem. Soc., Dalton Trans.* **2000**, 3885–3896.

[35] P.-E. Car, M. Perfetti, M. Mannini, A. Favre, A. Caneschi, R. Sessoli, *Chem. Commun.* **2011**, *47*, 3571–3573.

[36] D.-P. Li, X.-P. Zhang, T.-W. Wang, B.-B. Ma, C.-H. Li, Y.-Z. Li, X.-Z. You, *Chem. Commun.* **2011**, *47*, 6867–6869.

[37] L. Rigamonti, A. Cornia, A. Nava, M. Perfetti, M.-E. Boulon, A.-L. Barra, X. Zhong, K. Park, R. Sessoli, *Phys. Chem. Chem. Phys.* **2014**, *16*, 17220–17230.

[38] N. F. Chilton, D. Collison, E. J. McInnes, R. E. Winpenny, A. Soncini, *Nature Commun.* **2013**, *4*.

[39] L. F. Chibotaru, L. Ungur, *J. Chem. Phys.* **2012**, *137*, 064112.

[40] S. Xue, L. Ungur, Y.-N. Guo, J. Tang, L. F. Chibotaru, *Inorg. Chem.* **2014**, *53*, 12658–12663.

[41] G. Cosquer, F. Pointillart, S. Golhen, O. Cador, L. Ouahab, *Chem. Eur. J.* **2013**, *19*, 7895–7903.

[42] E. Bartolomé, J. Bartolomé, S. Melnic, D. Prodius, S. Shova, A. Arauzo, J. Luzón, F. Luis, C. Turta, *Dalton Trans.* **2013**, *42*, 10153–10171.

[43] L. Norel, K. Bernot, M. Feng, T. Roisnel, A. Caneschi, R. Sessoli, S. Rigaut, *Chem. Commun.* **2012**, *48*, 3948–3950.

[44] H. B. G. Casimir, F. K. Du Pré, *Physica* **1938**, *5*, 507–511.

[45] D. Gatteschi, R. Sessoli, J. Villain, *Molecular Nanomagnets*, Oxford University Press, **2006**.

[46] M. Gregson, N. F. Chilton, A.-M. Ariciu, F. Tuna, I. F. Crowe, W. Lewis, A. J. Blake, D. Collison, E. J. McInnes, R. E. Winpenny, S. T. Liddle, *Chem. Sci.* **2016**, *7*, 155–165.

[47] J. M. Zadrozny, M. Atanasov, A. M. Bryan, C.-Y. Lin, B. D. Rekken, P. P. Power, F. Neese, J. R. Long, *Chem. Sci.* **2013**, *4*, 125–138.

[48] S. Demir, J. M. Zadrozny, J. R. Long, *Chem. Eur. J.* **2014**, *20*, 9524–9529.

[49] A. Abragam, B. Bleaney, *Electron Paramagnetic Resonance of Transition Ions*, Oxford University Press, **1970**.

[50] L. Ungur, M. Thewissen, J.-P. Costes, W. Wernsdorfer, L. F. Chibotaru, *Inorg. Chem.* **2013**, *52*, 6328–6337.

[51] F. Pointillart, K. Bernot, S. Golhen, B. Le Guennic, T. Guizouarn, L. Ouahab, O. Cador, *Angew. Chem.* **2015**, *127*, 1524–1527.

[52] C. Das, A. Upadhyay, S. Vaidya, S. K. Singh, G. Rajaraman, M. Shanmugam, *Chem. Commun.* **2015**, *51*, 6137–6140.

[53] N. F. Chilton, C. A. Goodwin, D. P. Mills, R. E. Winpenny, *Chem. Comm.* **2015**, *51*, 101–103.

[54] K. S. Pedersen, L. Ungur, M. Sigrist, A. Sundt, M. Schau-Magnussen, V. Vieru, H. Mutka, S. Rols, H. Weihe, O. Waldmann, L. F. Chibotaru, J. Bendix, J. Dreiser, *Chem. Sci.* **2014**, *5*, 1650–1660.

[55] Q.-W. Li, J.-L. Liu, J.-H. Jia, J.-D. Leng, W.-Q. Lin, Y.-C. Chen, M.-L. Tong, *Dalton Trans.* **2013**, *42*, 11262–11270.

[56] J. Ruiz, G. Lorusso, M. Evangelisti, E. K. Brechin, S. J. Pope, E. Colacio, *Inorg. Chem.* **2014**, *53*, 3586–3594.

[57] S. Gómez-Coca, A. Urtizberea, E. Cremades, P. J. Alonso, A. Camón, E. Ruiz, F. Luis, *Nature Commun.* **2014**, *5*.

[58] J.-P. Costes, C. Duhayon, L. Vendier, *Inorg. Chem.* **2014**, *53*, 2181–2187.

[59] A. Altomare, G. Cascarano, C. Giacovazzo, A. Guagliardi, *J. Appl. Crystallogr.* **1993**, *26*, 343–350.

[60] G. Sheldrick, *SHELXL-97, program for X-ray crystal structure refinement*, **1997**.

[61] L. J. Farrugia, *J. Appl. Crystallogr.* **1999**, *32*, 837–838.

[62] D. Moss, *Acta Crystallogr. Sect. A* **1975**, *31*, 877–878.

[63] F. Aquilante, L. De Vico, N. Ferré, G. Ghigo, P.-å. Malmqvist, P. Neogrády, T. B. Pedersen, M. Pitoňák, M. Reiher, B. O. Roos, L. Serrano-Andrés, M. Urban, R. Lindh, *J. Comput. Chem* **2010**, *31*, 224–247.